Supporting Information

Achieving high thermoelectric Performance of Triple Half-Heusler Compositions Enabled by High-Throughput Screening

Kazuki Imasato[1*], Haruhiko Morito[2], Hidetoshi Miyazaki[3], Fumikazu Hosono[4], Philipp Sauerschnig[1], Masanobu Miyata[1], Takao Ishida[1], Atsushi Yamamoto[1], Yukari Katsura[4], Michihiro Ohta[1]

[1] Global Zero Emission Research Center, National Institute of Advanced Industrial Science and Technology (AIST), Tsukuba, Ibaraki 305-8569, Japan

[2] Institute for Materials Research, Tohoku University, Sendai, Japan

[3] Department of Physical Science and Engineering, Nagoya Institute of Technology, 466-8555, Nagoya, Japan

[4] Center for Basic Research on Materials, National Institute for Materials Science (NIMS), Tsukuba, Japan

email: kazuki-imasato@aist.go.jp

[*] Corresponding Author

Figure S1-S9 shows XRD results of high throughput synthesis. Sample ID corresponding to each composition can be found in Table S1.

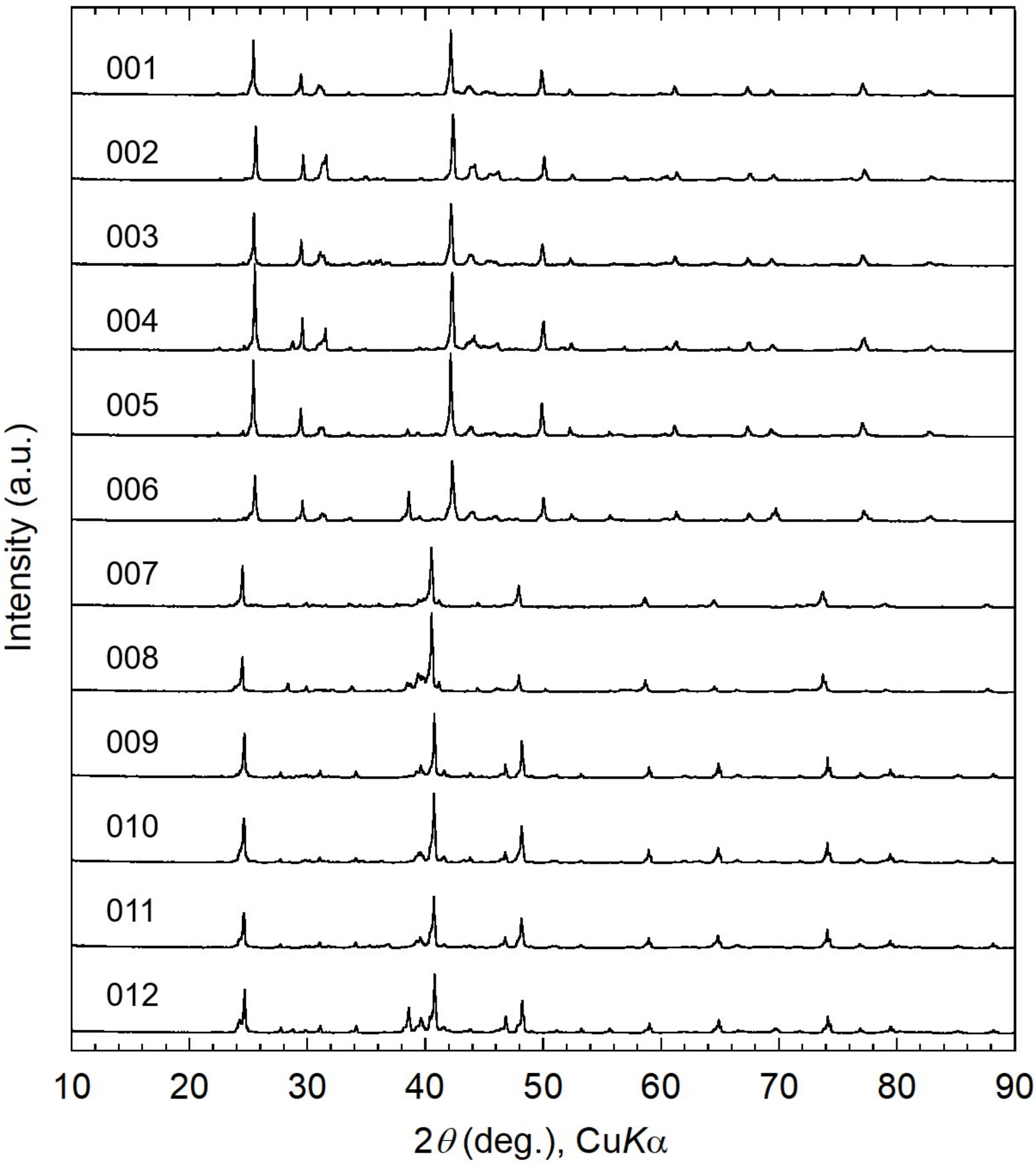

Fig. S1 XRD patterns of Mg-based alloys (SID: 001–012)

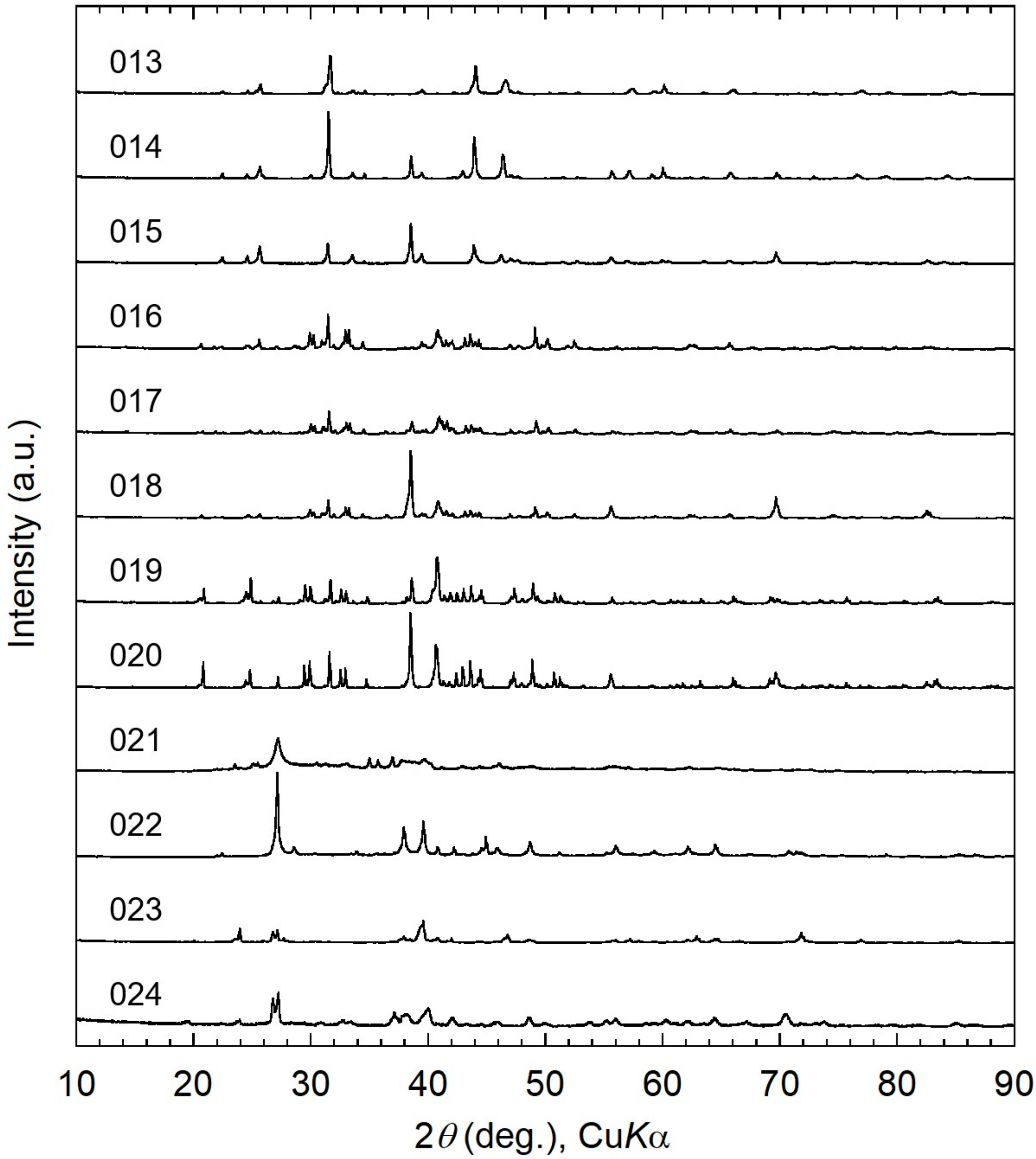

Fig. S2 XRD patterns of Mg-based alloys (SID: 013–024)

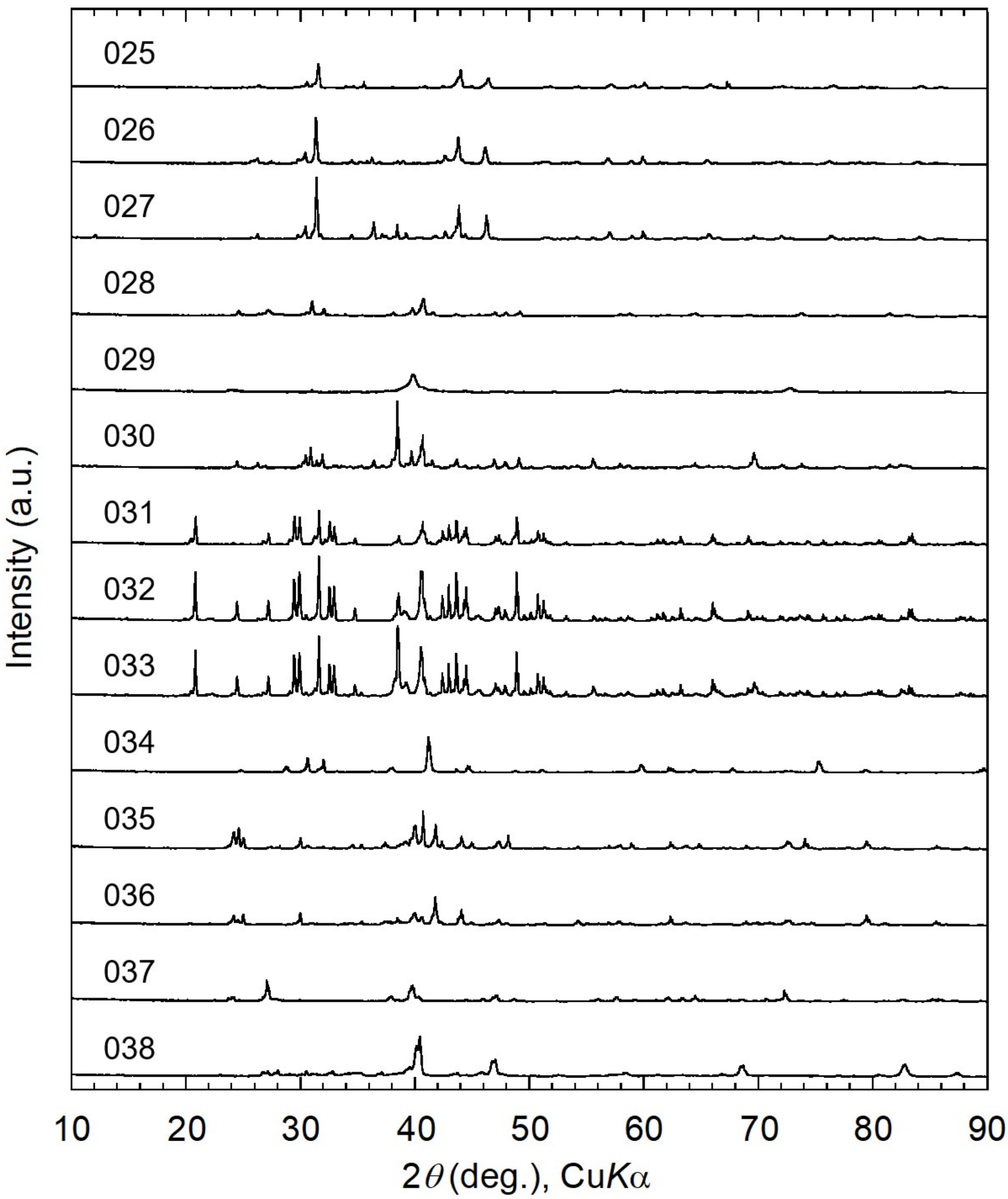

Fig. S3 XRD patterns of Sc-based alloys (SID: 025–038)

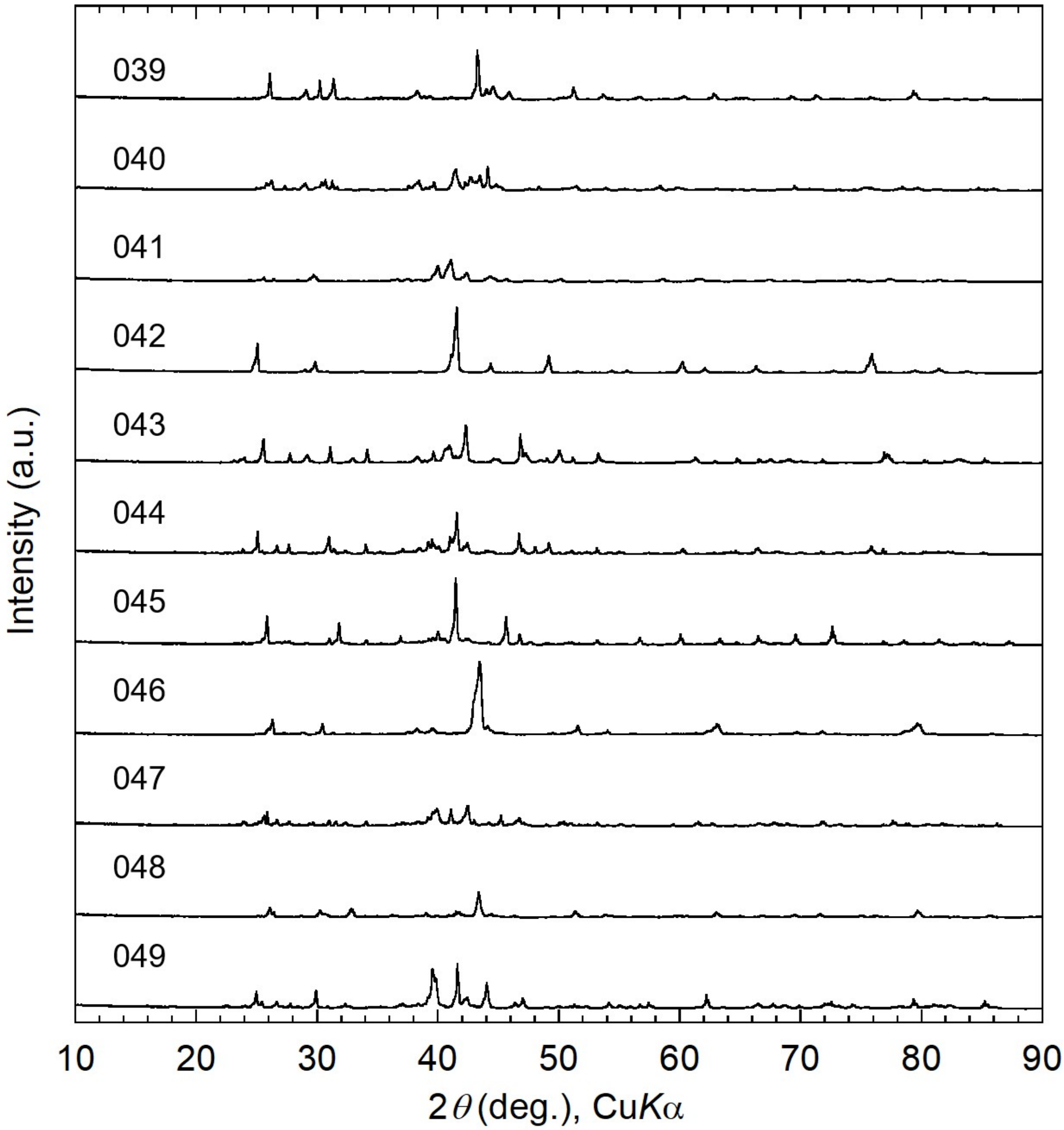

Fig. S4 XRD patterns of Ti-based alloys (SID: 039–049)

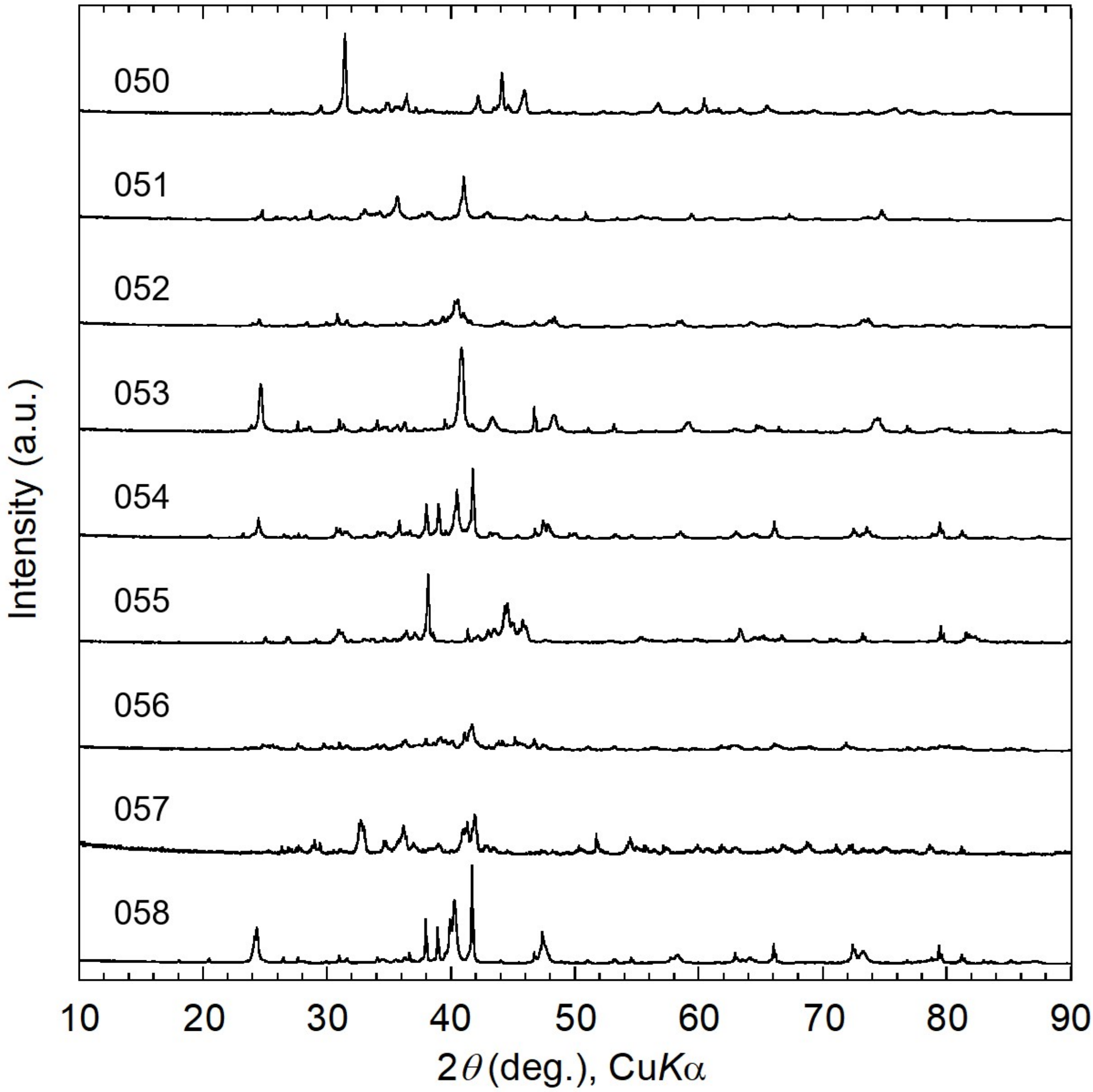

Fig. S5 XRD patterns of Zr-based alloys (SID: 050–058)

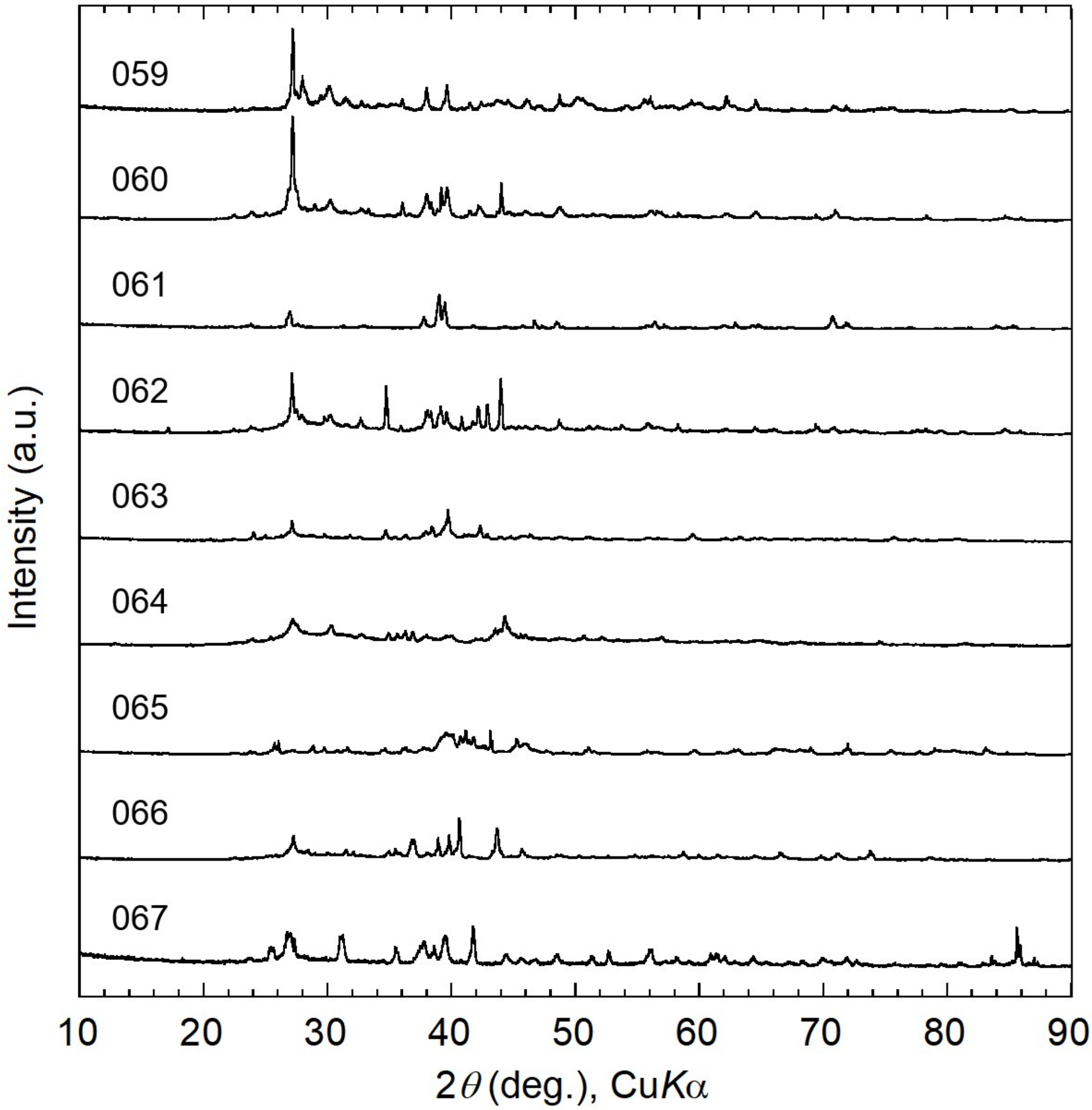

Fig. S6 XRD patterns of Zr-based alloys (SID: 059–067)

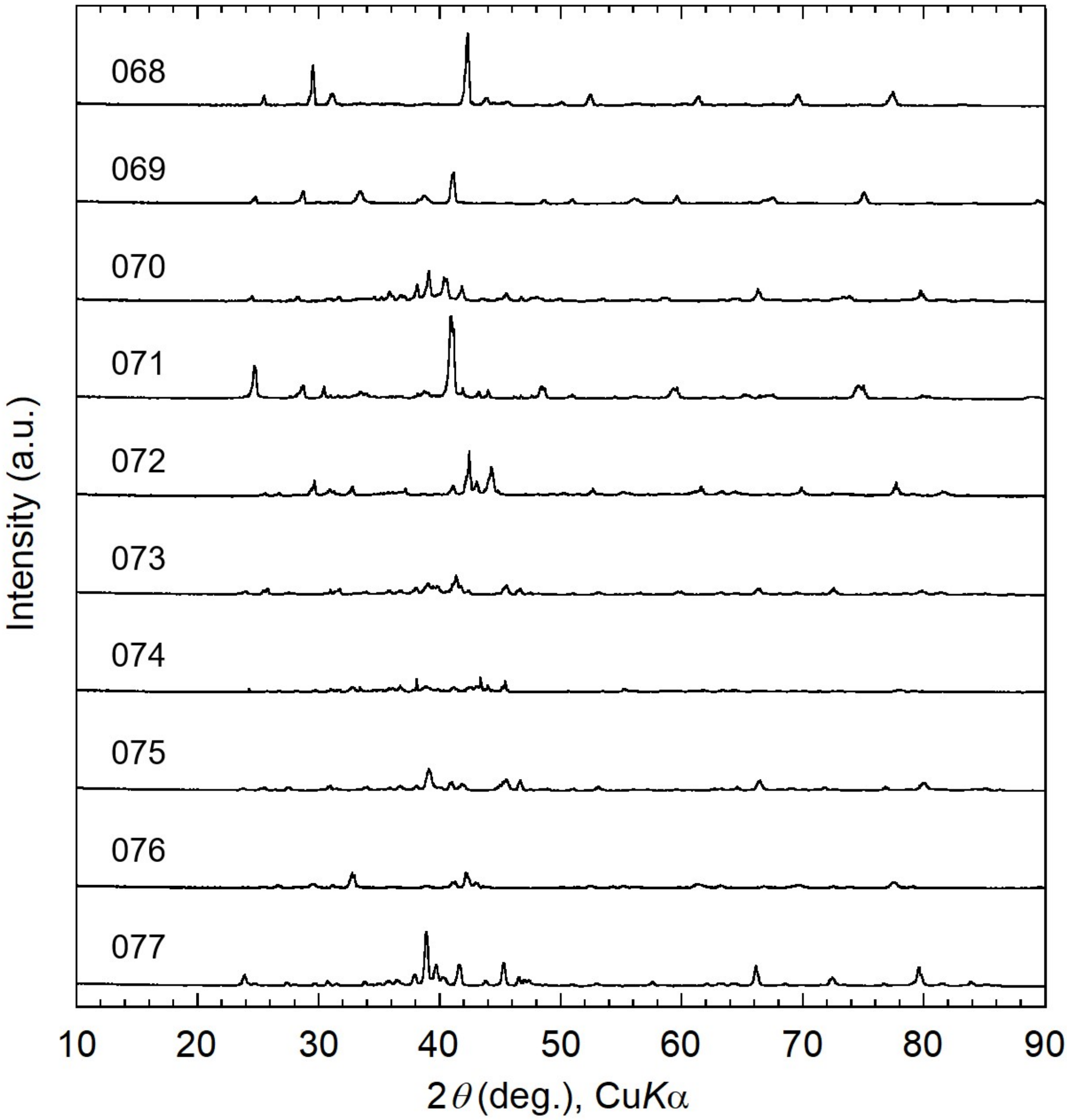

Fig. S7 XRD patterns of Hf-based alloys (SID: 068–077)

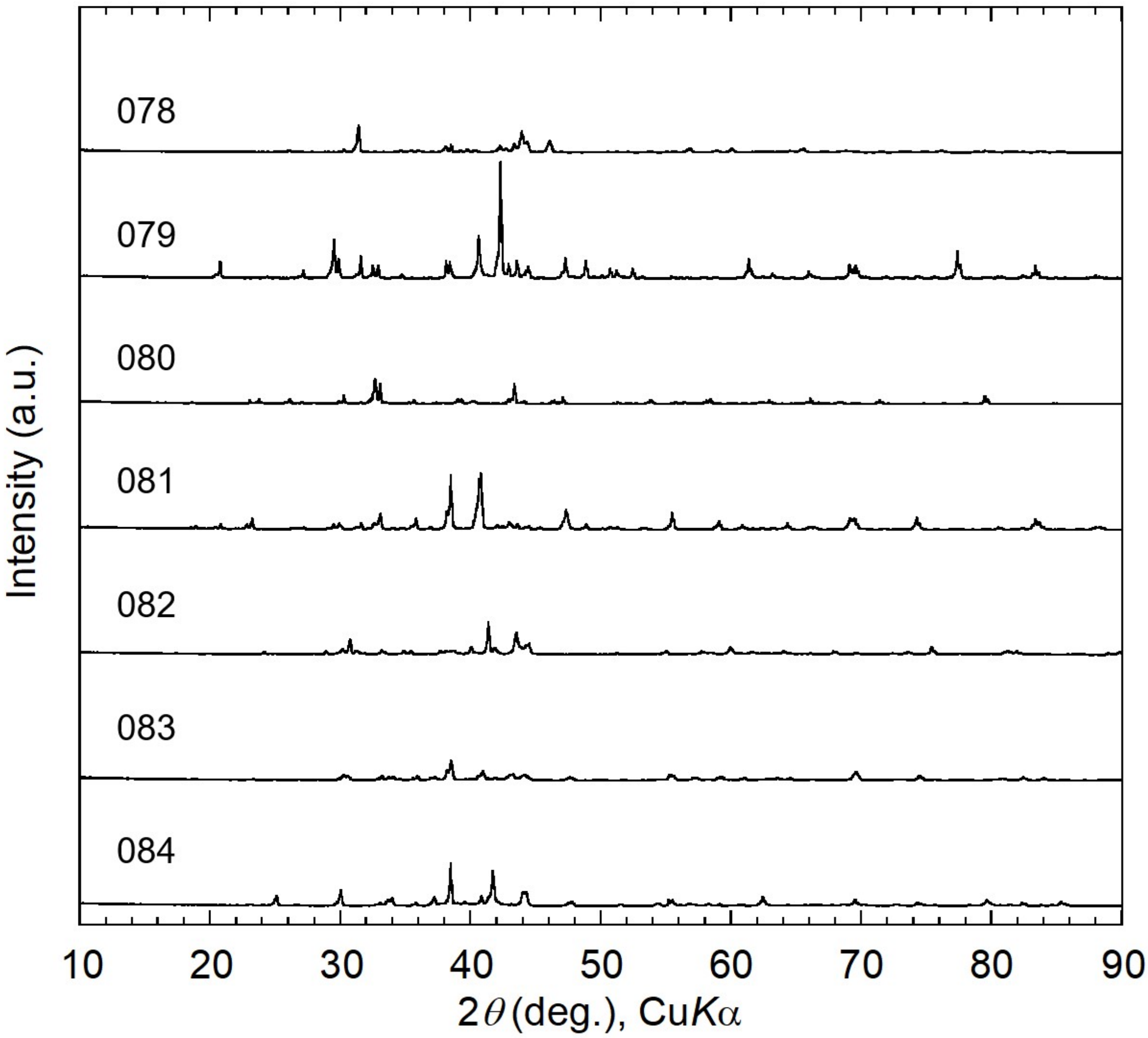

Fig. S8 XRD patterns of Nb-based alloys (SID: 078–084)

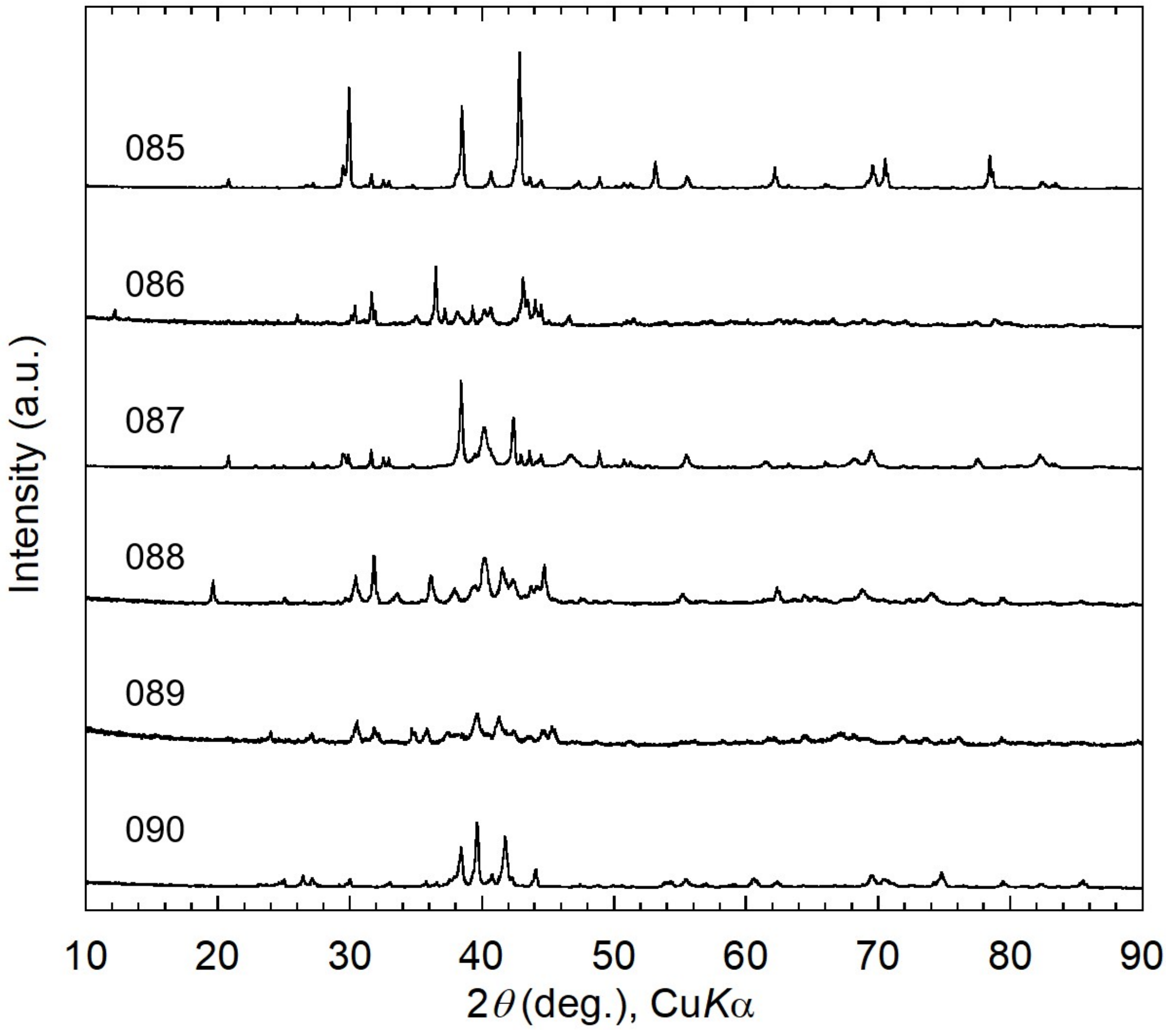

Fig. S9 XRD patterns of Ta-based alloys (SID: 085–090)

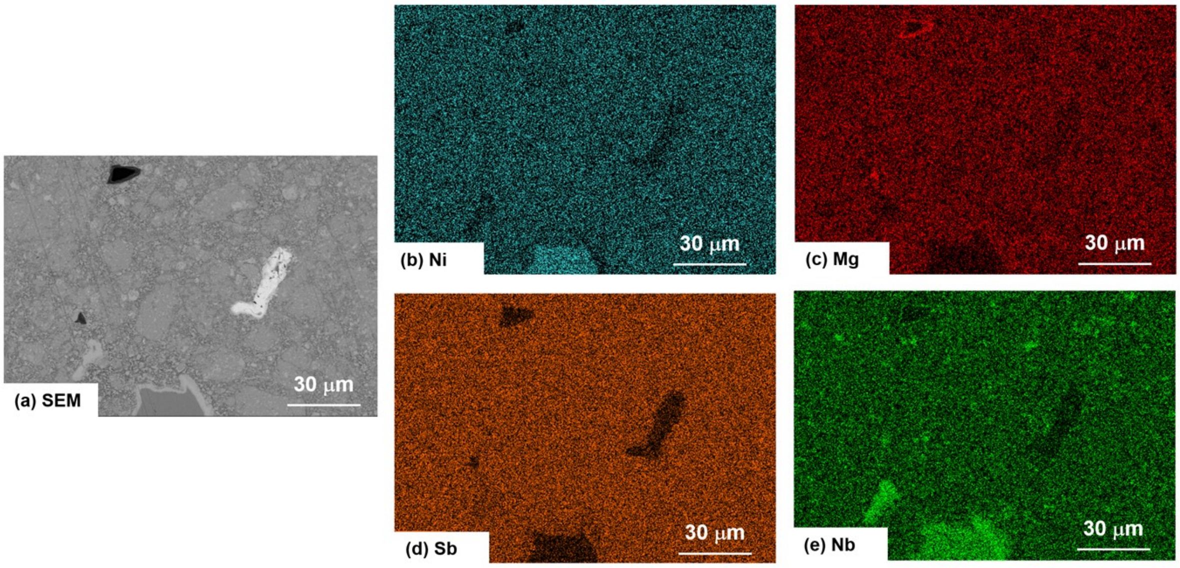

Fig. S10 (a) SEM image of synthesized $Mg_2NbNi_3Sb_3$ bulk sample. EDS mapping of $Mg_2NbNi_3Sb_3$ showed the compositional distribution of (b)Ni, (c) Mg, (d) Sb, and (e) Nb. There are some unreacted impurity phases such as Nb-rich and Ni-rich phases.

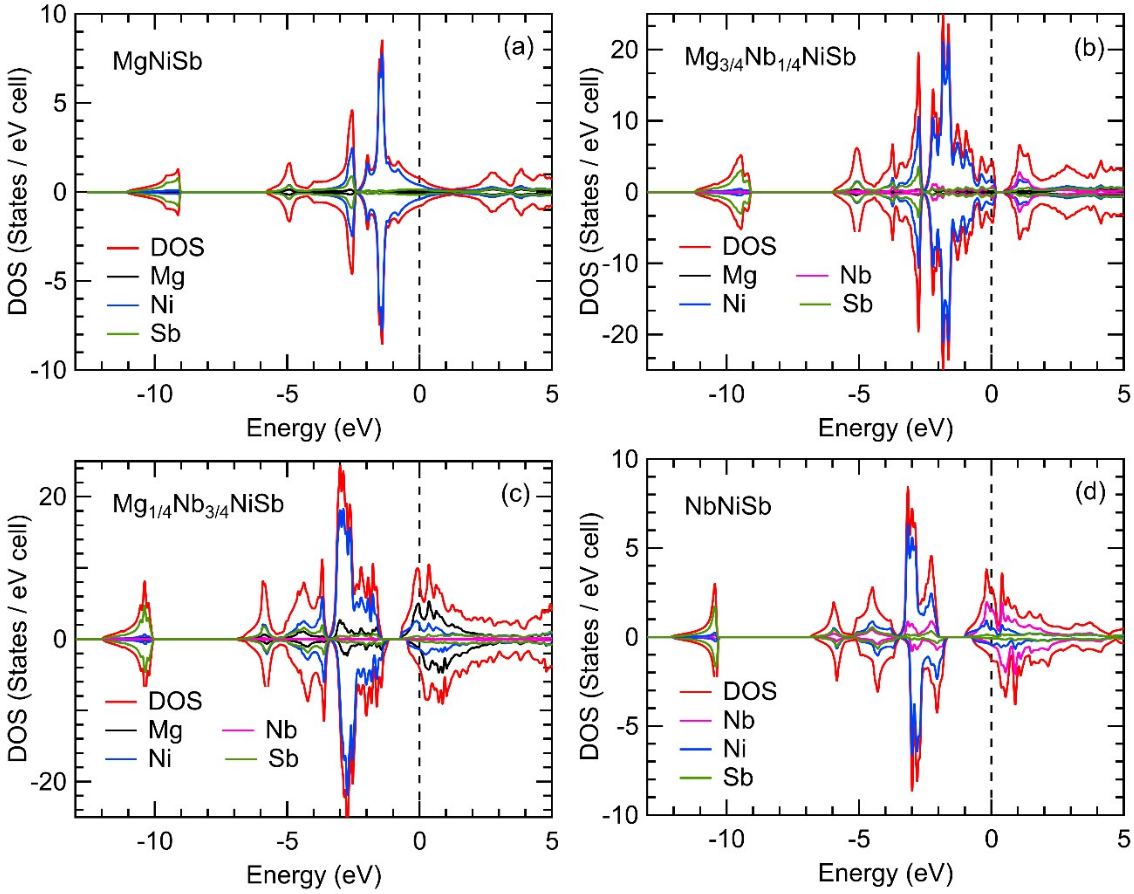

Figure S11 density functional theory (DFT) calculations of MgNiSb, NbNiSb, $Mg_{1/4}Nb_{3/4}NiSb$, and $Mg_{3/4}Nb_{1/4}NiSb$

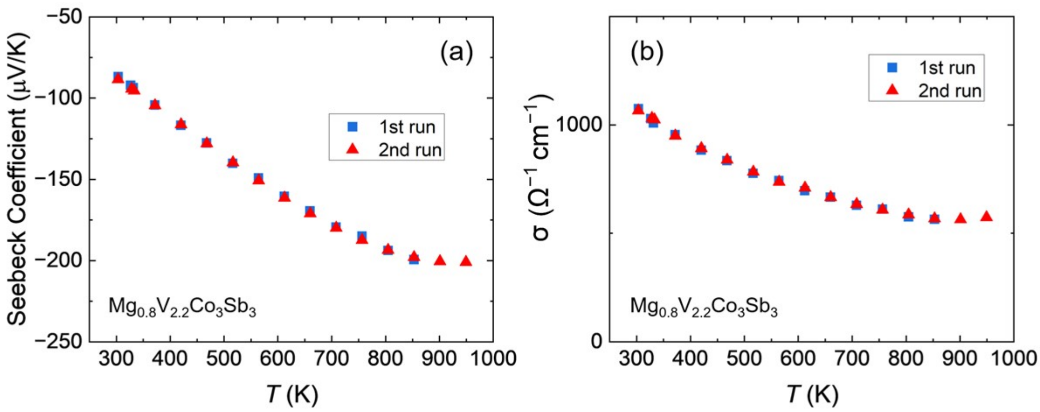

Fig. S12 Repetitive measurement of Seebeck coefficient and electrical conductivity on $Mg_{0.8}V_{2.2}Co_3Sb_3$ (x=0.2 sample) showing the stability of these compositions up to 950 K.

Summary of structural stability

To investigate the stability of the Mg–V–Co–Sb and Mg–Nb–Ni–Sb based compounds, first-principles calculations were performed using the Vienna Ab initio Simulation Package (VASP) [1, 2]. The generalized gradient approximation (GGA) in the Perdew–Burke–Ernzerhof (PBE) form was employed for the exchange–correlation functional, and the projector augmented-wave (PAW) method was used to describe the electron–ion interactions. A plane-wave cutoff energy of 520 eV was applied in all calculations. Brillouin zone integrations were carried out using Monkhorst–Pack k-point meshes of 11 × 11 × 11.

For geometry optimizations, both lattice parameters and internal atomic positions were fully relaxed until the forces on each atom were smaller than [specify, e.g., 0.001 eV/Å] and the residual stress was less than 0.1 GPa. The formation energies were determined from the total energy differences between the compounds and their constituent elements in the stable reference phases (Mg: hcp, V: bcc, Nb: bcc, Co: hcp, Ni: fcc, Sb: A7). Cohesive energies were calculated relative to the energies of isolated atoms obtained in large vacuum cells with spin polarization. These energy-based quantities were used to evaluate the relative stability of the studied compounds.

The independent elastic constants were determined by the stress–strain method (SSM). Small symmetry-allowed strains were applied to the equilibrium structures in the range of −1.0% to +1.0% (−0.01, −0.006, −0.003, 0.003, 0.006, and 0.01), and the resulting stress tensors were calculated by VASP. The elastic constants were then obtained from linear fits of stress–strain relations. Bulk, shear, and Young's modulus, as well as Poisson's ratio, were derived from the calculated elastic constants using the Voigt–Reuss–Hill averaging scheme. These mechanical parameters provide complementary insight into the mechanical stability of the compounds.

Phonon dispersion relations and phonon density of states (DOS) were calculated using the finite-displacement method as implemented in the Phonopy code [3]. Supercells of size 2×2×2 were constructed from the fully relaxed equilibrium structures, and small atomic displacements of 0.01 Å were introduced. The interatomic forces were obtained from VASP calculations using the same plane-wave cutoff and exchange–correlation functional as in the total-energy calculations. For Brillouin zone sampling, Monkhorst–Pack k-point meshes were reduced in proportion to the supercell size, ensuring that the k-point density was equivalent to that of the primitive cell calculations. The phonon spectra were then obtained by Fourier transforming the calculated force constants.

Table S1 shows the equilibrium lattice constants, formation energies, and cohesive energies obtained from VASP calculations after full structural relaxation. In terms of energetic stability, all studied Mg–V–Co–Sb and Mg–Nb–Ni–Sb compounds exhibit negative formation energies, indicating that they are thermodynamically stable with respect to decomposition into the constituent elements.

Structurally, in the Mg–V–Co–Sb and Mg–Nb–Ni–Sb compounds, the lattice constant systematically increases with increasing Mg content, consistent with the atomic-size contrast at the substituted site (Mg versus V/Nb). This smooth, Vegard's-law-like variation also indicates that our DFT setup faithfully captures the chemical-substitution effect.

Table S2 shows the calculated elastic constants (C_{11}, C_{12}, C_{44}), bulk modulus (B), shear modulus (G), Young's modulus (E), and Poisson's ratio (v) for Mg–V–Co–Sb and Mg–Nb–Ni–Sb compounds. For cubic crystals, the Born mechanical stability criteria require that $C_{11} - C_{12} > 0$, $C_{11}+2C_{12} > 0$, and $C_{44} > 0$. All compounds studied here satisfy these conditions, confirming that they are mechanically stable.

The calculated bulk, shear, and Young's modulus in Mg–V–Co–Sb and Mg–Nb–Ni–Sb compounds decrease gradually with increasing Mg content, reflecting the weaker bonding associated with Mg substitution compared with V-rich compositions. The Poisson's ratios lie in the 0.27–0.40 range, consistent with balanced ductility versus brittleness. All compositions exhibit Pugh ratios $B/G >$ 1.75 (1.89–2.49 in the Mg–V–Co–Sb series and 1.79–4.63 in the Mg–Nb–Ni–Sb series), indicating intrinsically ductile behavior; the lowest B/G occurs for MgCoSb (~1.89) and $Mg_3Nb_1Ni_4Sb_4$ (~1.79), implying slightly reduced ductility relative to the other compositions.

Taken together, these results demonstrate that the Mg–V–Co–Sb and Mg–Nb–Ni–Sb compounds are not only mechanically stable according to the Born criteria but also possess favorable ductility, providing additional confirmation of their overall structural stability.

Fig. S13 shows the phonon dispersion relations (a1–d1) and phonon density of states (DOS) (a2–d2) for MgCoSb, $Mg_3V_3Co_4Sb_4$, $Mg_1V_3Co_4Sb_4$, and VNiSb. No imaginary phonon modes are observed across the Brillouin zone, confirming that all compounds are dynamically stable.

Fig. S14 shows the phonon dispersion relations (a1–d1) and phonon density of states (DOS) (a2–d2) for MgNiSb, $Mg_3Nb_1Ni_4Sb_4$, $Mg_1Nb_3Ni_4Sb_4$, and NbNiSb. No imaginary phonon modes are observed across the Brillouin zone, confirming that all compounds are dynamically stable for MgNiSb, $Mg_3Nb_1Ni_4Sb_4$. In contrast, $Mg_1NbNi_4Sb_4$ and NbNiSb exhibit branches dipping below zero frequency (imaginary modes in our plotting convention), indicating that the cubic half-Heusler phase is dynamically unstable at 0 K within the harmonic approximation.

We assessed stability from three complementary angles—thermodynamic, mechanical, and dynamical—using DFT. Thermodynamically, all studied compositions in the Mg–V–Co–Sb and Mg–Nb–Ni–Sb families show a driving force against decomposition into the elements, consistent with strong atomic binding. Mechanically, their elastic tensors satisfy the cubic Born criteria, and modulus trends place them in a generally ductile regime. Dynamically, most compositions display phonon spectra without imaginary modes at 0 K within the harmonic approximation; a limited subset shows soft/imaginary branches, suggesting a tendency toward symmetry lowering and/or finite-temperature (anharmonic) stabilization. In particular, the target compounds $Mg_3V_1Co_4Sb_4$ and $Mg_3Nb_1Ni_4Sb_4$ are found to be stable within DFT (0 K, harmonic approximation).

[1] Kresse, G., & Furthmüller, J. Comput. Mater. Sci. 6, 15–50 (1996).

[2] Kresse, G., & Furthmüller, J. Phys. Rev. B 54, 11169–11186 (1996)

[3] Togo, A., & Tanaka, I. Scr. Mater. 108, 1–5 (2015).

Table S1 Calculated equilibrium lattice constants a_0, formation energies E_{Form}, and cohesive energies E_{coh} (per atom) for VNiSb, $Mg_1V_3Ni_4Sb_4$, $Mg_3V_1Ni_4Sb_4$, and MgNiSb. All values are obtained from energy differences calculated by VASP.

	a_0 (Å)	E_{form} (eV/atom)	E_{coh} (eV/atom)
MgCoSb	6.0547	-0.1925	-3.3603
$Mg_3V_1Co_4Sb_4$	6.0064	-0.2536	-3.7475
$Mg_1V_3Co_4Sb_4$	5.8540	-0.2771	-4.4231
VCoSb	5.8285	-0.1863	-4.6585

	a_0 (Å)	E_{form} (eV/atom)	E_{coh} (eV/atom)
MgNiSb	6.0910	-0.4214	-3.4467
$Mg_3Nb_1Ni_4Sb_4$	6.0691	-0.4319	-3.9212
$Mg_1Nb_3Ni_4Sb_4$	6.0297	-0.1982	-4.6157
NbNiSb	6.0238	-0.0413	-4.9229

Table S2 Calculated elastic constants (C_{11}, C_{12}, C_{44}), bulk modulus (B), shear modulus (G), Young's modulus (E), and Poisson's ratio (n) for VNiSb, $Mg_1V_3Ni_4Sb_4$, $Mg_3V_1Ni_4Sb_4$, and MgNiSb. All values are obtained from f the stress–strain method using VASP.

	C_{11}	C_{12}	C_{44}	B (GPa)	G (GPa)
MgCoSb	154.46	56.59	46.19	89.15	47.28
$Mg_3V_1Co_4Sb_4$	159.74	61.14	46.56	94.01	47.64
$Mg_1V_3Co_4Sb_4$	224.64	90.04	53.74	134.91	58.80
VCoSb	235.35	93.00	48.16	140.45	56.34

	E (GPa)	n
MgCoSb	120.54	0.274
$Mg_3V_1Co_4Sb_4$	122.26	0.283
$Mg_1V_3Co_4Sb_4$	154.03	0.310
VCoSb	149.10	0.323

	C_{11}	C_{12}	C_{44}	B (GPa)	G (GPa)
MgNiSb	139.19	54.75	40.14	82.89	40.96
$Mg_3Nb_1Ni_4Sb_4$	163.85	59.58	53.19	94.34	52.77
$Mg_1Nb_3Ni_4Sb_4$	188.85	92.02	38.07	124.30	41.92
NbNiSb	199.17	107.670	22.30	138.17	29.86

	E (GPa)	n
MgNiSb	105.50	0.288
$Mg_3Nb_1Ni_4Sb_4$	133.43	0.264
$Mg_1Nb_3Ni_4Sb_4$	113.04	0.348
NbNiSb	83.57	0.399

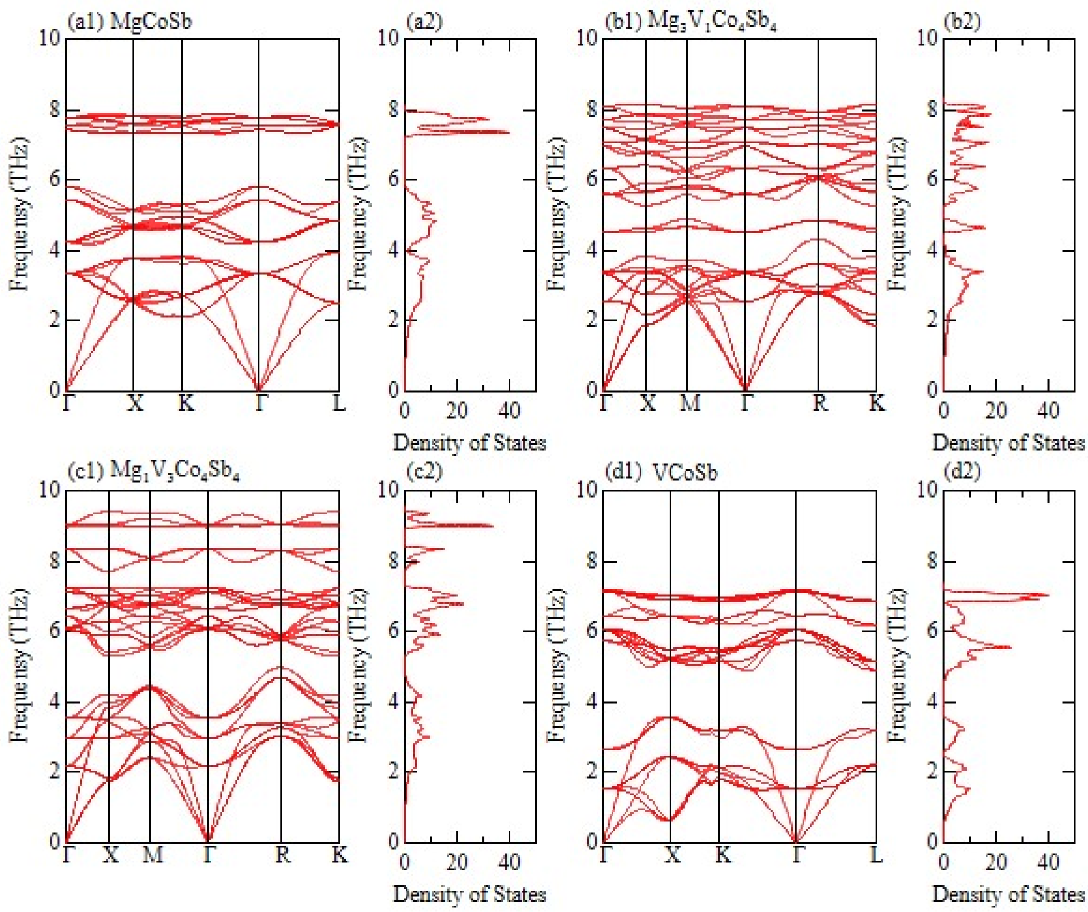

Fig. S13. Phonon dispersion relations (a1–d1) and phonon density of states (a2–d2) for MgCoSb, $Mg_3V_1Co_4Sb_4$, $Mg_1V_3Co_4Sb_4$, and VCoSb. All calculations are performed by Phonopy and VASP.

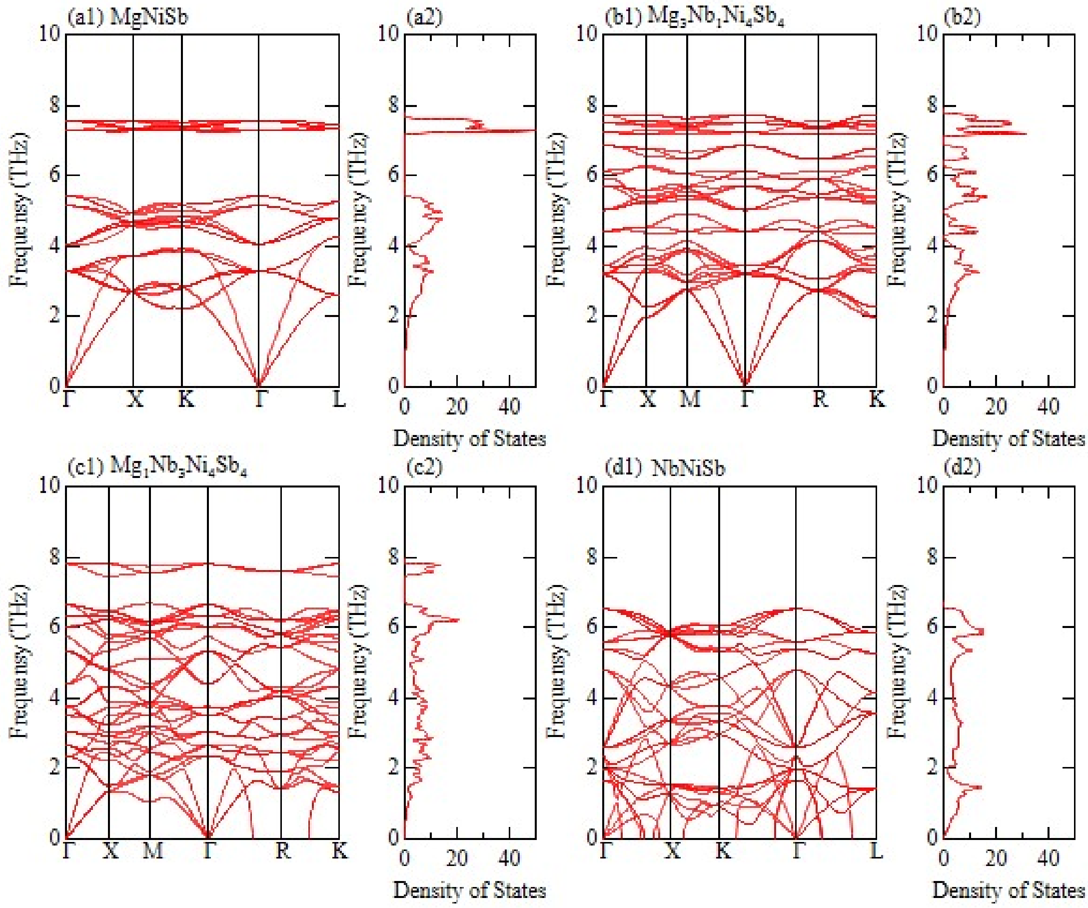

Fig. S14. Phonon dispersion relations (a1–d1) and phonon density of states (a2–d2) for MgNiSb, $Mg_3Nb_1Ni_4Sb_4$, $Mg_1Nb_3Ni_4Sb_4$, and NbNiSb. All calculations are performed by Phonopy and VASP.